

# Extinction of high-power laser radiation under adverse weather conditions

ANDREAS PECKHAUS,<sup>1,\*</sup>  PETER BECKER,<sup>2</sup> CARSTEN PARGMANN,<sup>3</sup> THOMAS HALL,<sup>1</sup>  
AND FRANK DUSCHEK<sup>2</sup> 

<sup>1</sup>German Aerospace Center (DLR), Institute of Technical Physics, Pfaffenwaldring 38-40, 70569 Stuttgart, Germany

<sup>2</sup>German Aerospace Center (DLR), Institute of Technical Physics, Langer Grund, 74239 Hardthausen, Germany

<sup>3</sup>Heilbronn University of Applied Sciences, Faculty of Mechanics and Electronics, Max-Planck-Straße 39, 74081 Heilbronn, Germany

\*andreas.peckhaus@dlr.de

Received 26 May 2023; revised 17 August 2023; accepted 17 August 2023; posted 18 August 2023; published 11 September 2023

The propagation of laser radiation over long distances can be significantly affected by atmospheric extinction due to precipitation as well as aerosol particles and molecules. The knowledge of the contribution of precipitation is critical to the operation of a variety of laser-based systems. The study of high-power laser transmission around 1  $\mu\text{m}$  is of particular interest because several atmospheric transmission windows are located in this region. To investigate the effect of adverse weather conditions on laser transmission, free-space laser transmission experiments are conducted on the DLR test range in Lampoldshausen, Germany. A high-power laser with a wavelength of 1.03  $\mu\text{m}$  is used for the transmission measurements in combination with calibrated power monitors. Local weather conditions are continuously monitored by meteorological instruments during the experiments. Extinction coefficients are derived from transmission measurements showing that the extinction for snow is 7 times higher than for rain, and the extinction for drizzle/rain is 4 times higher than for rain at a given precipitation rate of 1 mm/h. For a mixture of rain and snow, the extinction is comparable to that of rain, indicating that the water content strongly influences the optical properties and thus the extinction of laser radiation in mixed precipitation. A good relationship is found between the measured extinction coefficient and visibility for drizzle and rain and a slightly larger scatter of the data for snow. Furthermore, measured extinction coefficients are compared to the extinction coefficients based on the experimental size distributions of precipitation particles and geometric optics. A reasonable agreement is obtained for rain, with no improvement taking the forward-scattering into the detector aperture into account, and a much better agreement is obtained for snow when the forward-scattering contribution is included.

Published by Optica Publishing Group under the terms of the [Creative Commons Attribution 4.0 License](https://creativecommons.org/licenses/by/4.0/). Further distribution of this work must maintain attribution to the author(s) and the published article's title, journal citation, and DOI.

<https://doi.org/10.1364/AO.496443>

## 1. INTRODUCTION

The performance of laser-based systems can be significantly affected by adverse weather conditions. In particular, precipitation, along with aerosol particles and molecules in the atmosphere can lead to the extinction of laser radiation due to scattering and absorption, resulting in a reduced operation range and SNR of the detection systems [1,2]. The knowledge of atmospheric extinction plays a key role in many outdoor laser applications, such as free-space optical communications links [3], imaging via lidar [4], and in the field of defense-related research [5,6]. Accordingly, there is an ongoing demand to determine the transmission of laser radiation under real atmospheric conditions and to establish simple but reliable estimates for the atmospheric extinction coefficient based on routinely recorded meteorological parameters.

Numerous studies have addressed the extinction of laser radiation propagating through the atmosphere in the presence of liquid and solid precipitation [7–17]. The extinction coefficient has been linked to various observable parameters such as the precipitation rate, visibility range, and size distributions of liquid and solid hydrometeors. Empirical relations for the extinction in rain indicate that there is a comparatively consistent relation between the extinction coefficient and the liquid precipitation rate [12,18,19]. The extinction coefficient increases nonlinearly with the precipitation rate, with a factor of 2–3 variation in the extinction for a given precipitation rate. In contrast, a factor of 10–15 higher extinction is reported for snow at a given precipitation rate [20]. However, Seagraves emphasizes that a single empirical relation between the extinction coefficient and the solid precipitation rate cannot be established unless additional dependencies are considered [14]. For example, the falling velocity of different snow types [1], the wind-induced drift of

snow near the instrument [1,21], and the presence of fog during snowfall [20,22] are mentioned as affecting the empirical relation between the extinction in snow and the solid precipitation rate.

The extinction coefficient and visibility are inversely related via the Koschmieder equation [23]. Several formulations have been reported for snow that deviate from the original Koschmieder equation [22]. An approximate approach to determine the extinction due to snow has been proposed by Seagraves, which considers the diffraction of snow particles [15]. A more complex method is to use the size distribution of precipitation particles to calculate the extinction coefficient. Simulated and parameterized size distributions are used to calculate the extinction coefficients for rain and snow [3,12]. On the other hand, it has been shown that the extinction can be calculated directly from the measured size distributions of snow particles [4].

The measurement of extinction coefficients is impaired by the fact that there is a spectral dependence of the extinction in rain and snow [10,16,17]. This spectral dependence is attributed to the diffraction pattern of precipitation particles because a significant portion of the scattered radiation can enter the detector's field-of-view (FOV) in the forward direction and thereby reduce the extinction coefficient [10]. This effect is frequently accounted for by approximating the forward-scattering with the Fraunhofer diffraction theory [10,24] or by fitting a Gauss function to the forward-scattering lobe of the phase function [7,25]. Apart from forward-scattering, additional corrections of the extinction coefficient based on the radiative transfer theory can be made for multiple scattering at high particle number densities [10,17]. Extensive extinction measurement data under precipitation conditions are available for the visible and IR regions (i.e., 0.63, 3.5, and 10.6  $\mu\text{m}$ ) [7–9]. However, experimental studies on the transmission of laser radiation around 1  $\mu\text{m}$ , which focus on the relation between laser transmission and observable weather parameters are sparse [11,16,26]. The wavelength around 1  $\mu\text{m}$  is interesting because there are several atmospheric transmission windows in this region. In particular, low water vapor absorption coefficients occur in the range between 0.95 and 1.1  $\mu\text{m}$ , where the emission spectrum of the high-power laser operating at a wavelength of 1.03  $\mu\text{m}$  is located [27]. For this reason, an experimental study on laser transmission has been conducted on the German Aerospace Center (DLR) laser test range that not only focuses on the relation with observable weather parameters, but also puts forward a detailed comparison with the calculated extinction coefficient derived from measured size distributions and geometric optics.

The study has five sections. In the second section, theoretical background of the atmospheric extinction coefficient and the relationship to the observable weather parameters such as the precipitation rate and visibility are described. The third section presents the experimental setup for the transmission experiments and the accompanying meteorological instrumentation. The fourth section deals with the results of the transmission experiments. The empirical relations of the extinction coefficient with observable parameters under rainy and snowy conditions are presented. This information is followed by a detailed comparison of the measured extinction coefficients and the calculated extinction coefficients based on the measured size

distributions of precipitation particles and geometric optics. The study closes with a summary of the main findings.

## 2. THEORETICAL BACKGROUND

### A. Calculation of Extinction Coefficients

The extinction of electromagnetic radiation passing through a particulate atmosphere can be described by the Beer–Lambert law [28] as

$$dP = -\beta_{\text{ext}} P ds, \quad (1)$$

where  $dP$  is the differential change in the radiant power in the infinitesimal path length  $ds$ ,  $P$  is the radiant power, and  $\beta_{\text{ext}}$  is the extinction coefficient. The extinction coefficient is the sum of the scattering and absorption coefficient of atmospheric constituents. Equation (1) can be integrated from the initial radiant power  $P_0$  at  $s = 0$  to the radiant power  $P$  at the end of the path length  $s$ . After rearranging, an expression for the extinction coefficient can be obtained by

$$\beta_{\text{ext}} = -\frac{1}{s} \ln \left( \frac{P}{P_0} \right). \quad (2)$$

The application of Eq. (2) involves certain assumptions: The distribution of atmospheric particles is homogeneous and isotropic along the propagation path. The concentration is assumed not to vary, so Eq. (1) can be integrated over the path length, resulting in a path-averaged extinction value. The concentration of atmospheric scatterers is considered low, such that the inter-particle distance is sufficiently large to be in the single-scattering regime. At higher concentrations of atmospheric scatterers and optically dense scattering media, collective effects such as multiple scattering must be taken into account [25]. Corrections for forward-scattered light due to the measurement geometry of transmission experiments are addressed below.

An equivalent expression for the extinction coefficient is obtained from the number size distribution and the extinction cross-section  $\sigma_{\text{ext}}(m, \alpha)$  of atmospheric particles [28] by

$$\beta_{\text{ext}} = \int_{D_{\min}}^{D_{\max}} \sigma_{\text{ext}}(m, \alpha) n(D_i) dD_i, \quad (3)$$

where  $D_{\min}$  and  $D_{\max}$  are the upper and lower limits of the particle diameters,  $n(D_i)dD_i$  is the number of particles per unit volume with diameters in the range  $D_i$  to  $D_i + dD_i$ ,  $\alpha$  is the size parameter (given by  $\alpha = \frac{\pi D_i}{\lambda}$ ), and  $m$  is the complex refractive index of the particles. Equation (3) can be rewritten in terms of the extinction efficiency factor  $Q_{\text{ext}}(m, \alpha)$  and the geometrical cross-section of the particles as

$$\beta_{\text{ext}} = \int_{D_{\min}}^{D_{\max}} \frac{\pi D_i^2}{4} Q_{\text{ext}}(m, \alpha) n(D_i) dD_i. \quad (4)$$

For the numerical calculation of the extinction coefficients, Eq. (4) is converted from a continuous to a discrete number size distribution and each extinction efficiency factor is multiplied by the corresponding number concentration of atmospheric particles to get

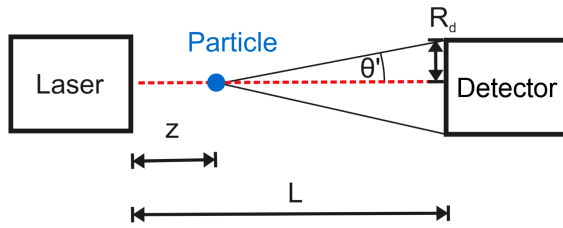


**Fig. 1.** Schematic drawing of the open detector transmission system.  $\theta'$  denotes the half angle subtended by the detector as seen from the position of the particle.  $z$  and  $L$  are the distances from the laser to the particle or the detector, respectively.  $R_d$  denotes the radius of the detector aperture.

$$\beta_{\text{ext}} = \sum_{i=1}^k \frac{\pi D_i^2}{4} Q_{\text{ext}}(m, \alpha) n(D_i). \quad (5)$$

The extinction efficiency factors  $Q_{\text{ext}}$  are routinely calculated based on the Mie theory [29]. In the size regime where the atmospheric particles are much larger than the wavelength, the geometric optics approximation can be applied. The extinction efficiency factor is therefore close to 2.0.  $Q_{\text{ext}}$  is reported to be within 1% of the asymptotic value of  $Q_{\text{ext}} \approx 2.0$  for large precipitation particles [30].

Due to the particle size and the detection geometry, forward-scattered radiation of precipitation particles can reach the FOV of the detector and thus reduce the measured extinction coefficient. To account for the amount of forward scattering, the extinction coefficient can be corrected based on the Fraunhofer diffraction theory [10,15] by

$$Q_{\text{ext}}' = Q_{\text{ext}} - 2\pi \int_0^{\theta'} \frac{J_1^2(\alpha \sin \theta)}{\pi \sin^2 \theta} \sin \theta d\theta \\ = Q_{\text{ext}} - [1 - J_0^2(\alpha \sin \theta') - J_1^2(\alpha \sin \theta')], \quad (6)$$

where  $J_0$  and  $J_1$  are Bessel functions of the first kind and of orders zero and one, respectively,  $\theta'$  is the half-angle of the scattered light cone in the forward direction (defined by  $\theta' = \arctan(R_d/(L-z))$ ,  $R_d$  is the radius of the detector,  $L$  is the distance between the transmitter and the receiver, and  $z$  is the distance between the transmitter and the position of the particle on the beam axis. A schematic illustration of the scattering geometry is given in Fig. 1.

The corrected extinction efficiency factor  $Q_{\text{ext}}'$  is substituted into Eq. (5) to obtain the corrected extinction coefficient. The correction is applied to the extinction coefficient calculated from the measured size distributions and geometric optics to ensure comparability to the measured extinction coefficient values.

When applying the forward-scattering correction, the precipitation particles are assumed to be spherical in shape. For drizzle and small raindrops below 1 mm, this assumption seems reasonable [31]. However, larger raindrops are flattened on the bottom as they fall through the atmosphere, resulting in deviations from the spherical shape. In particular, snow is a highly nonspherical material composed of irregularly shaped grains [32]. Bohren and Koh pointed out that the spherical shape approximation can lead to an error of about 20% in the

correction factor for needle-shaped snow crystals and large detector apertures [33].

## B. Size Distribution of Precipitation Particles

The number size distribution can be obtained by size and velocity-resolved measurements of hydrometeors by

$$n(D_i) = \sum_{j=1}^k \frac{N_{ij}}{A_i \Delta t v_j \Delta D_i}, \quad (7)$$

where  $D_i$  is the particle diameter of the  $i$ th bin,  $n(D_i)$  is the number of precipitation particles per unit volume and per class width in the range  $D_i$  to  $D_i + \Delta D_i$ ,  $N_{ij}$  is the absolute number of particles in size bin  $i$  and velocity bin  $j$ ,  $A_i$  is the effective sampling area,  $\Delta t$  is the sampling interval,  $v_j$  is the falling velocity of the particles,  $\Delta D_i$  is the size class width depending on the particle diameter, and  $k$  is the total number of velocity bins [34]. It should be noted that the measured number size distribution of particles is normalized by the class widths  $\Delta D_i$  of the instrument.  $n(D_i)$  has units of  $\text{m}^{-3} \text{mm}^{-1}$  due to this normalization.

A gamma-type distribution is widely used to represent the number size distribution of precipitation particles as

$$n(D) = n_0 D^\mu e^{-\Lambda D}, \quad (8)$$

where  $n_0$  is the intercept on the ordinate,  $\Lambda$  is the slope of the size distribution,  $\mu$  is the order of the gamma distribution (i.e., shape parameter), and  $D$  is the particle diameter. Equation (8) has been used to fit measured size distributions of liquid and solid precipitation particles [12,35].  $n(D)$  in Eqs. (7) and (8) has the units of particle numbers per unit volume per unit size interval (i.e.,  $\text{m}^{-3} \text{mm}^{-1}$ ) [12].

## C. Relationship to Precipitation Rate

The extinction coefficient of the precipitation particles can be related to the precipitation rate. The general expression for the precipitation rate  $R_p$  is given by

$$R_p = \int_{D_{\min}}^{D_{\max}} \left( \frac{\pi D_i^3}{6} \right) v(D_i) n(D_i) D_i. \quad (9)$$

Alternative forms of Eq. (9) to numerically calculate the precipitation rate based on size and velocity measurements of precipitation particles can be found in [34,36]. Empirical power law approaches are used to relate the extinction coefficient and the precipitation rate. The parameterization of the extinction coefficient can be expressed as

$$\beta_{\text{ext}} = a R_p^b, \quad (10)$$

where  $a$  and  $b$  are coefficients and exponents, respectively, that can be obtained from the nonlinear fitting of experimental data. The derived parameters depend on the meteorological and experimental conditions.

### D. Relationship to Visibility

The meteorological visibility in the daytime is another observable parameter that can be related to the measured extinction coefficient. The relation between the extinction coefficient and the visibility can be formulated as

$$\beta_{\text{ext}} = \frac{\ln(1/C_V)}{V}, \quad (11)$$

where  $C_V$  is the contrast threshold value of the human eye. Equation (11) is referred to as the Koschmieder equation, in which a contrast threshold value of 2% is assumed [23]. Present visibility meters (and the one applied in this work) use a contrast threshold value of 5% by default, resulting in a numerator of 3.0 in Eq. (11) [37]. The visibility data relies on the extinction coefficient measurements, which are subsequently converted to the visual range (i.e., 0.55  $\mu\text{m}$ ), where the human eye has its maximum visual sensitivity.

## 3. EXPERIMENT

### A. Laser Transmission Experiments

Laser transmission measurements are performed on the DLR laser test range at Lampoldshausen. The details of the optical setup and the laser system have been described previously [38,39]. Briefly, a diode-pumped disk laser (TruDisk 6001 (4C), Trumpf, Ditzingen, Germany) with a wavelength of 1.03  $\mu\text{m}$  is used for the transmission measurements. The laser emits cw unpolarized radiation in the range of 0.18–6 kW. The laser radiation is fed into an optical fiber and guided to the transmitting station (TS). At the TS, the laser beam is expanded to obtain a tenfold increase in the beam diameter at the exit aperture. A fraction of the laser beam is directed to the power monitor (CPM F-1, PRIMES GmbH, Pfungstadt, Germany) for power measurements via an optical wedge and an off-axis parabolic mirror before the beam is sent out to the laser test range. After the exit aperture, the laser beam propagates a 130 m long horizontal path, 1 m above the ground, to the receiving station (RS). The laser beam has a diameter of 2–3 cm at the end of the laser test range in the RS. The RS is similarly equipped with a power monitor (CPM F-20, PRIMES GmbH) for power measurements. The power monitors are calibrated with equipment and methods traceable to the Physikalisch-Technische Bundesanstalt (PTB), the national metrology institute in Germany. The power monitors are free aperture detectors with a

diameter of 135 mm (in the case of the CPM F-20) and no collection optics are used in front of the detectors. In addition, fast power measurements are performed using an integrating sphere (819D-GL-6, Newport Corp., Irvine, CA, USA) coupled to a calibrated photodiode (PDA 10CS-EC, Thorlabs, Newton, NJ, USA) for the purpose of correlation with angle-resolved scattering measurements [39] that are not part of this study. The acquisition frequency of the power monitor and the photodiode are 1 Hz and 500 Hz, respectively. The manufacturer of the power monitors specifies the accuracy with  $\pm 3\%$  and the reproducibility with  $\pm 1.5\%$  [40]. A schematic representation of the experimental setup is shown in Fig. 2.

Laser transmission measurements were carried out between Feb. 4, 2016, and March 22, 2018. The measurement duration was between 15 and 30 min for each experiment. The laser output power was set to 3 kW for the majority of the experiments, but 5 kW also was tested. The measurements were performed to cover different weather conditions, including drizzle, rain, snow, and mixed precipitation.

### B. Meteorological Instrumentation

The transmission measurements are accompanied by atmospheric sensing instruments located on the DLR laser test range. A geographic map with the locations of the instruments is included in Appendix A (see Fig. 9). Here is a brief description of the equipment:

1. A laser precipitation monitor (LPM, 5.4110.00.200, Adolf Thies GmbH & Co. KG, Göttingen, Germany) measures the size and velocity of precipitation particles in the range of 0.18–8.25 mm and 0.2–20 m/s, respectively, resulting in 440 ( $22 \times 20$ ) classes. The sampling time is 60 s and the measuring area is 0.00456  $\text{m}^2$ . The laser precipitation monitor provides the precipitation rate in the range of <0.005 to >250 mm/h. The error in the precipitation rate is  $\leq 15\%$  for rain and  $\leq 30\%$  for snow, according to the specifications of the manufacturer [41]. The surface synoptic observation (SYNOP) weather code (Table 4680) recommended by the World Meteorological Organization (WMO) is issued by the laser precipitation monitor and used for the discrimination of the precipitation types (see Section 4.A). A description of the classification algorithm and the exact calculation of the precipitation rate is unfortunately not provided by the manufacturer [4,21].

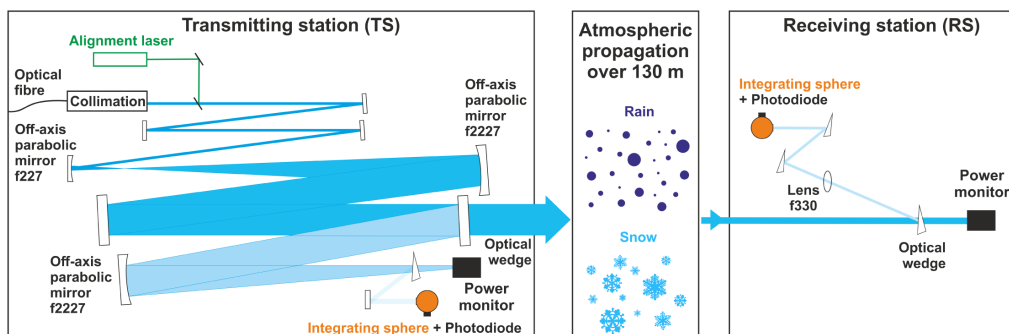


**Fig. 2.** Schematic representation of the experimental setup used for the transmission experiments on the DLR laser test range at Lampoldshausen.



2. A forward scatterometer (FSM, VPF-730, Biral, Portishead, UK) detects the scattered light in the angular range of  $39^{\circ}$ – $51^{\circ}$  (centered at  $45^{\circ}$ ) and provides meteorological visibility. The visibility is given for the range of 0.01–75 km. The accuracy of the visibility measurements is specified by the manufacturer with  $\pm 2\%$  at 2 km,  $\pm 10\%$  at 16 km, and  $\pm 20\%$  from 16 to 30 km [42]. The instrument can distinguish haze and fog in the presence or absence of precipitation via the ratio of the back-scatter to forward-scatter coefficient and the environmental conditions.
3. An aerosol spectrometer (Fidas 200S, Palas GmbH, Karlsruhe, Germany) measures the scattered light of single aerosol particles suspended in the atmosphere in a  $90^{\circ}$  detection geometry. The number size distribution of aerosol particles is determined for the range of 0.18–18.44  $\mu\text{m}$ , yielding a total of 65 size classes.

In addition, several weather sensors monitor the ambient air temperature, relative humidity, wind direction, and speed on the laser test range, as shown in Table 1. All instruments record meteorological data every minute (24/7), which are stored on a hard disk.

### C. Data Post-processing

For post-processing of the transmission measurements, the readings from the power monitors are restricted to the range of interest, in which constant output power is achieved, taking into account the instrument-specific rise and fall times. The transmission is calculated from the power values, which is subsequently smoothed with a Savitzky–Golay (GS) filter (50-point window) and interpolated to 1-minute intervals. This processing is chosen to reduce noise, but preserve data characteristics and ensure comparability with observable data from other instruments. The transmission values are converted to extinction coefficients according to Eq. (2).

The precipitation rate and visibility data are taken unchanged from the instrument's internal software. In the case of mixed precipitation, the total precipitation rate is used; otherwise, the liquid or solid precipitation rate. The size- and velocity-resolved data of the laser precipitation monitor are not filtered, following the study by Fehlmann *et al.* [21]. In that study, a filtering procedure was not applied to the raw data for two reasons: (1) The measurements were performed at low wind speeds (i.e., less than 20 m/s), and (2) the contribution of filtered-out particles to the total volume was estimated to be small. Since the measurement conditions are similar to those of Fehlmann *et al.*, no filtering of the raw data is performed in this study. The conversion to the number size distributions is done according to Eq. (7). In the end, the measured extinction coefficients are related to the aggregated one-minute data of the observable parameters (i.e., precipitation rate and visibility) and compared to the calculated extinction coefficients, according to Eq. (5).

## 4. RESULTS AND DISCUSSION

### A. Laser Transmission Experiments

An overview of the average weather and laser transmission parameters measured during the experiments is given in Table 1. The type of precipitation during the laser transmission experiments is classified into drizzle/rain, rain, and snow based on the most frequent SYNOP code figure during the experiments; i.e., the dominant precipitation type provided by the Thies laser precipitation monitor [43]. It becomes apparent that light precipitation conditions are investigated for the different types of precipitation. The average precipitation rate for each measurement series is below 2.5 mm/h [44], with occasional higher precipitation rate values. The average temperatures range from  $13.5^{\circ}\text{C}$  to  $14.3^{\circ}\text{C}$  for drizzle/rain, from  $1.9^{\circ}\text{C}$  to  $7.7^{\circ}\text{C}$  for rain, and from  $0.1^{\circ}\text{C}$  to  $2.7^{\circ}\text{C}$  for snow. The relative humidity is elevated, which is to be expected for precipitation conditions. In most experiments, the average visibility is above 1 km, with the exception of one snow event (Exp. #18) where the average visibility was 0.8 km. The average total aerosol concentration for each measurement series is in the range of 10–427 particles per  $\text{cm}^3$ . Higher values for the total aerosol concentration are encountered for snow compared to the other precipitation types. The average transmission and measured extinction coefficients are between 77.0% and 99.0%, and between 0.08 and  $2.01 \text{ km}^{-1}$ , respectively.

Figure 3 shows an exemplary time series of laser transmission, visibility, and precipitation rate for drizzle/rain and snow. It can be seen that the laser transmission and visibility are positively related, while the laser transmission and precipitation rate are negatively related. Due to the aggregation of data on a common 1-minute basis, longer-lasting trends can be seen, but changes that occur on a shorter timescale are not resolved.

### B. Relationship to Precipitation Rate

Figure 4 shows the extinction coefficient as a function of the precipitation rate for the different precipitation types; i.e., drizzle/rain, rain, and snow. Generally, the extinction coefficient increases nonlinearly with an increasing precipitation rate. Higher extinction coefficients are observed for drizzle/rain compared to rain, as shown in the left panel of Fig. 4. For a precipitation rate of 1 mm/h, the extinction due to drizzle/rain is a factor of four times higher than due to rain. This finding is corroborated by visibility measurements indicating significantly lower visibilities and thus higher extinction coefficients for drizzle compared to rain for a given precipitation rate [45]. The higher number concentrations and smaller particle sizes of drizzle droplets [46] are likely related to the difference in the extinction of the precipitation types, as shown in Fig. 5. The extinction coefficients for snow are higher than those for drizzle/rain and rain, as shown in the right panel of Fig. 4. For a precipitation rate of 1 mm/h, the extinction due to snow is a factor of seven times higher than due to rain. O'Brien's study supports this observation by noticing that the extinction due to snow can be about an order of magnitude higher than for rain [20]. A flattening of the extinction coefficient for snow with an increasing precipitation rate is also observed in previous investigations [14,22].

**Table 1. Overview of the Parameters Measured during the Laser Transmission Experiments<sup>a</sup>**

Exp.#	Exp. ID	T [°C]	RH [%]	V [km]	$R_p$ [mm/h]	SYNOP <sup>b,c</sup> code	$n_{\text{Aerosol}}$ <sup>d</sup> [# / cm <sup>3</sup> ]	T [%]	$\beta_{\text{ext}}$ [km <sup>-1</sup> ]
1	08/10/2017_1056	14.3	96.8	12.2	0.13	<b>51/52/57</b>	148	96.0	0.32
2	08/10/2017_1327	13.6	98.0	2.5	2.04	<b>57/58</b>	58	84.1	1.33
3	08/10/2017_1414	13.7	98.2	2.4	2.24	<b>57/58</b>	45	83.6	1.38
4	08/10/2017_1502	13.7	98.2	3.9	0.67	<b>52/53/57</b>	21	88.7	0.92
5	08/10/2017_1600	13.5	98.0	2.9	1.35	<b>57/58</b>	28	85.8	1.18
6	02/04/2016_1130	1.9	96.0	7.1 <sup>e</sup>	1.78	<b>61/62/68</b>	—	93.6	0.51
7	03/13/2018_1542	7.4	86.8	29.4	0.22	<b>57/61</b>	73	98.4	0.13
8	03/13/2018_1602	7.3	86.1	42.0	0.16	<b>51/57/61</b>	80	99.0	0.08
9	03/16/2018_0904	6.6	87.3	17.0	0.58	<b>57/61</b>	164	97.4	0.20
10	03/16/2018_1302	7.7	95.1	12.0	1.04	<b>61</b>	131	96.9	0.24
11	03/20/2018_1301	0.1	75.9	6.1	0.28	<b>71</b>	227	87.2	1.07
12	03/20/2018_1321	0.9	69.4	25.7	0.01	<b>71/77</b>	232	97.6	0.18
13	03/22/2018_1350	1.2	88.7	12.2	0.05	<b>71/77</b>	348	96.8	0.25
14	03/22/2018_1435	1.4	90.0	4.9	0.14	<b>71</b>	351	90.4	0.77
15	03/22/2018_1457	1.0	93.2	5.0	0.07	<b>71</b>	350	90.3	0.78
16	03/22/2018_1517	0.9	94.0	2.7	0.49	<b>71</b>	401	83.6	1.38
17	03/22/2018_1536	0.7	95.1	2.1	1.07	<b>71/72</b>	427	79.2	1.79
18	02/23/2016_0923	0.4	98.8	0.8 <sup>e</sup>	1.70	<b>72</b>	—	77.0	2.01
19	04/19/2017_0954	1.5	93.3	14.8	0.03	<b>51/71/76</b>	168	92.3	0.62

<sup>a</sup>The data are arithmetic mean values of the parameters for each measurement series.

<sup>b</sup>The code figures are described in the manual on codes of the WMO [43]. These are the codes used in the table: 51, slight drizzle; 52, moderate drizzle; 53, heavy drizzle; 57, light drizzle with rain; 58, moderate/heavy drizzle with rain; 61, slight rain; 62, moderate rain; 68, rain/drizzle and snow; 71, light snow; 72, moderate snow; 76, diamond dust; and 77, snow grains.

<sup>c</sup>The bold code figure indicates the dominant SYNOP weather code for each measurement series.

<sup>d</sup>The total number concentration of aerosol particles is given in the range of 0.18–18  $\mu\text{m}$ .

<sup>e</sup>The visibility data is taken from the LPM because the FSM was not available.

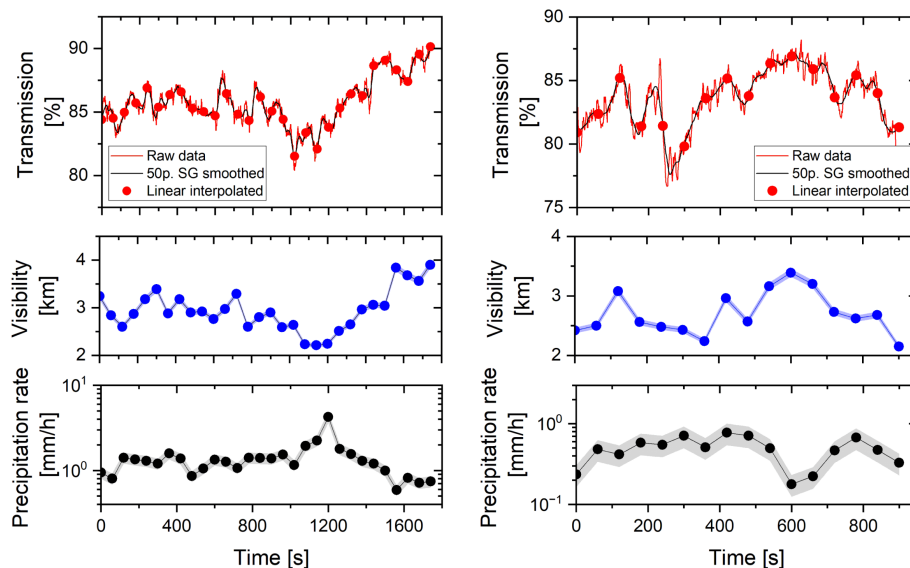


**Fig. 3.** Time series of the laser transmission (top panel), visibility (middle panel), and precipitation rate (bottom panel) for drizzle/rain (left side) and snow (right side). The measurements are from Aug. 10, 2017 (start time: 4 p.m.) on the left side and from March 22, 2018 (start time: 3:17 p.m.) on the right side. The uncertainty in visibility and precipitation rate is indicated by the shaded area.

The measurement data are parameterized using the power law relation in Eq. (10). For drizzle/rain, rain, and snow, the parameterizations are

$$\beta_{\text{ext}} = 0.29 R_p^{0.60}, \quad (12)$$

$$\beta_{\text{ext}} = 1.02 R_p^{0.41}, \quad (13)$$

$$\beta_{\text{ext}} = 1.71 R_p^{0.32}. \quad (14)$$

The corresponding  $r^2$  values of the parameterizations are 0.72, 0.88, and 0.81, respectively. For rain, the literature values for the coefficients and exponents range from 0.12 to 0.42 and from 0.46 to 0.82, respectively [12,18,19], as shown in Table 2. The fitting parameters fall within the range of the values in the

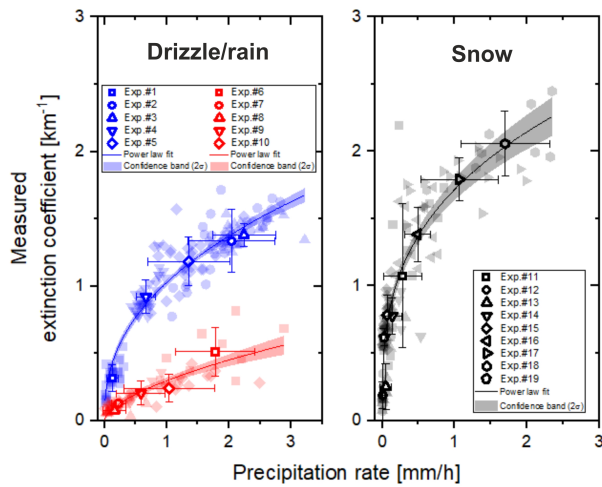


**Fig. 4.** Measured extinction coefficients as a function of precipitation rate for drizzle/rain (blue) and rain (red) in the left panel and snow (black) in the right panel. The transparent and open symbols are integrated one-minute measurements and arithmetic mean values for each measurement series, respectively. The error bars denote  $\pm 1$  standard deviation. The parameterizations are provided in the text.

literature. A good agreement is obtained with the parameterization of Chimelis, who derived the relation  $\beta_{\text{ext}} = 0.322 R_p^{0.6}$  from the transmission measurements of a carbon dioxide laser in rain over a wide range of precipitation rates [8].

For drizzle and rain, a detailed comparison is complicated, according to the available literature. However, Blanchard's parameterization ( $\beta_{\text{ext}} = 1.2 R_p^{0.33}$ ) for orographic rain can be used as a reference [48]. It has been pointed out that the parameterization is also applicable to drizzle [18]. The obtained parameterization for drizzle/rain is slightly lower than that of Blanchard, probably due to the simultaneous presence of rain and drizzle.

For snow, the literature values for the coefficients and exponents are in the range of 1.11 to 3.93 and 0.42 to 1, respectively [14,16,22], as shown in Table 3. The obtained parameterization for snow is consistent with the values in the literature. A greater variation in the parameter range can be recognized for snow, likely reflecting the different shapes and densities of snowflakes encountered during the experiments. Consequently, establishing an overall empirical power law relation between the extinction coefficient for snow and the solid precipitation rate is not appropriate [4]. A simple transfer of the results to other meteorological conditions (i.e., temperature and relative humidity) with different particle types and densities of snow is therefore not indicated [49].

### C. Relationship to Visibility

Figure 6 shows the extinction coefficient as a function of the visibility for drizzle/rain, rain, and snow. Note that the Koschmieder equation can be used to estimate the extinction due to liquid and solid precipitation based on visibility. However, there is a larger scatter in the visibility data for snow than for rain. The apparent discrepancies may be due to the forward scatterometer being calibrated in fog and haze and assuming similar applicability for rain and snow conditions,

**Table 2.** Overview of the Empirical Relations for the Extinction Coefficient as a Function of the Liquid Precipitation Rate<sup>a</sup>

Reference	Classification <sup>b</sup>	<i>a</i>	<i>b</i>
As reported by Atlas [18]:			
Ynyslas (1950)	PSD	0.25	0.64
Shoeburness (1950)	PSD	0.16	0.61
Lenard (1904)	PSD	0.17	0.57
Laws and Parsons (1943)	PSD	0.24	0.68
Marshall and Palmer (1948, Best)	PSD	0.35	0.64
East Hill (1950)	PSD	0.22	0.56
Hilo (Hawaii)	PSD (non-orographic)	0.33	0.55
Blanchard (1952)	PSD (non-orographic)	0.18	0.70
Blanchard (1952)	PSD (orographic)	1.27	0.33
Cambridge, Mass.	PSD	0.20	0.68
As reported by Shipley <i>et al.</i> [19]:			
Atlas (1953)	PSD (MP)	0.31	0.67
Best (1950)	PSD	0.25	0.61
Chu and Hogg (1968)	Ext. (0.63/3.5/10.6)	0.18	0.67
Miller (1973)	PSD	0.12	0.78
Poliakova (1960)	PSD	0.21	0.74
Simms and Mueller (1972)	PSD	0.13	0.82
Wessels (1972)	PSD	0.25	0.59
As reported by Ulbrich and Atlas [12]:			
Shipley (1974)	Ext. (0.69)	0.16	0.74
Winchester (1982)	Ext. (0.63/1.06/8-12)	0.31	0.47
Winchester (1983)	Ext. (0.63/1.06/8-12)	0.25	0.62
Chu and Hogg (1968)	Ext. (0.63/3.5/10.6)	0.42	0.46
Nedvidek <i>et al.</i> (1983)	Ext. (0.92)	0.16	0.76
Ulbrich and Atlas (1985)	Combined data	0.21	0.68
Ulbrich and Atlas (1977)	Ext. (Vis/Microwave)	0.18	0.69
[47]			
Chimelis (1982) [8]	Ext. (10.6)	0.32	0.60
Rensch and Long (1970)	Ext. (0.63/10.6)	0.42	0.50
[9]			
This study (rain)	Ext. (1.03)	0.29	0.60
This study (drizzle/rain)	Ext. (1.03)	1.02	0.41

<sup>a</sup>The empirical relation has the form  $\beta_{\text{ext}} = a R_p^b$ , where *a* is in units of  $\text{km}^{-1}$  and *b* is dimensionless.

<sup>b</sup>PSD refers to the measurement of the size distribution of rain droplets from which the  $\beta_{\text{ext}}(R_p)$  relationship can be derived, and Ext. refers to extinction experiments at specified wavelengths (in  $\mu\text{m}$ ) and the correlation with precipitation rate measurements using meteorological instruments.

even though this involves larger uncertainties in the visibility. The forward scatterometer detects scattered light at a given angle and then converts it to a visible extinction coefficient under the assumptions of a known phase function and negligible absorption [42]. The phase function is associated with uncertainties because its variations depend on the size and shape of the precipitation particles [11]. In addition, a small measurement volume is sampled by the forward-scattering instrument compared to the integrated output of the transmission measurements over the path length, which can lead to deviations.

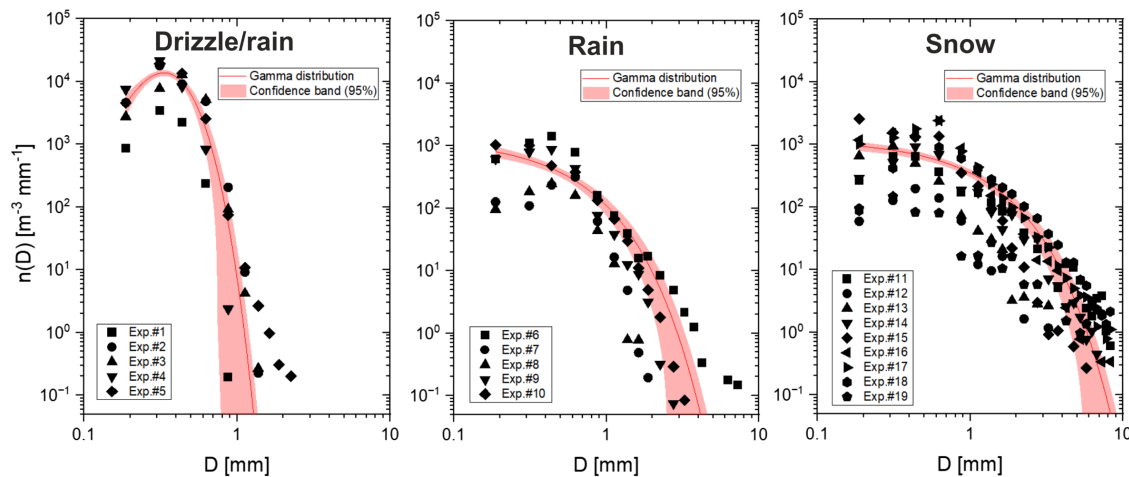


**Fig. 5.** Number size distributions of precipitation particles. Left panel: drizzle/rain; middle panel: rain; and right panel: snow. The parameterizations of the gamma-type distributions are given in Section 4.D.

**Table 3. Overview of the Empirical Relations for the Extinction Coefficient as a Function of the Solid Precipitation Rate<sup>a</sup>**

Reference	Classification <sup>b</sup>	<i>a</i>	<i>b</i>
As reported by Mason [22]:			
Lillesaeter (1965)	Ext. (0.45)	3.93	1.0
Zel'monovich (1960)	Ext. (3.87)	1.3	0.5
Poljakova and Tretjakov (1960)	Ext. (Vis)	3.2	0.91
Mellor (1966)	Ext. (Vis)	1.11	0.42
Warner and Gunn (1969)	Ext. (0.45)	2.53	1.0
O'Brien (1970)	Ext. (Vis)	1.39	0.69
As reported by Seagraves [14]:			
O'Brien (1970)	Ext. (Vis)	2.90	0.69
Bisyrarin <i>et al.</i> (1971)	Ext. (0.63)	2.49	0.53
Muench and Brown (1977)	Ext. (Vis)	2.52	0.77
As reported by Koh [16]:			
Lillesaeter (1965)	Ext. (0.45)	4.1	1.0
O'Brien (1970)	Ext. (Vis)	3.1	1.0
Nishitsuji and Matsumoto (1971)	Ext. (Radio/Microwave)	1.9	1.0
Koh (1989)	Ext. (Vis/1.06/3-5/8-14)	1.5–7.0	1.0
This study (snow)	Ext. (1.03)	1.71	0.32

<sup>a</sup>The empirical relation has the form  $\beta_{\text{ext}} = a R_p^b$ , where *a* is in units of  $\text{km}^{-1}$  and *b* is dimensionless.

<sup>b</sup>Ext. refers to extinction experiments at specified wavelengths (in  $\mu\text{m}$ ) and the correlation with precipitation rate measurements using meteorological instruments.

#### D. Number Size Distributions of Precipitation Particles

Average values are derived from the measured 1-min particle size distributions for each measurement series. The size distributions for drizzle/rain, rain, and snow are shown in Fig. 5. Figure 5 shows that the size distribution for drizzle/rain is narrow with high particle number concentrations. The particle number concentrations have their maxima at around 0.3 mm. On the other hand, broad particle size distributions are observed for rain and snow. The raindrops have sizes in the range of 0.18–4 mm.

The picture looks different for snow, where snow particles up to 8.25 mm are measured. The size distribution of mixed precipitation (i.e., rain and snow) is similar to that of rain, with some particles with diameters  $>4$  mm appearing at the tail of the distribution, as shown in the right side of the middle panel in Fig. 5.

Curve-fitting of the measured size distributions using gamma-type distributions yielded the following parameters:  $n_0 = 5.4 \cdot 10^{11} \text{ m}^{-3} \text{ mm}^{-1-\mu}$ ,  $\mu = 8.32$ ,  $\Lambda = 25.02 \text{ mm}^{-1}$ , and  $r^2 = 0.77$  for drizzle/rain;  $n_0 = 1098.48 \text{ m}^{-3} \text{ mm}^{-1}$ ,  $\mu = 0$ ,  $\Lambda = 2.66 \text{ mm}^{-1}$ , and  $r^2 = 0.58$  for rain; and  $n_0 = 1177.39 \text{ m}^{-3} \text{ mm}^{-1}$ ,  $\mu = 0$ ,  $\Lambda = 1.21 \text{ mm}^{-1}$ , and  $r^2 = 0.51$  for snow. The shape parameter  $\mu$  is set to zero for rain and snow because many precipitation particle size distributions tend to follow the two-parameter exponential size distribution proposed by Marshall and Palmer [50]. The obtained fitting parameters  $n_0$  and  $\Lambda$  for rain and snow are in the range of values in the literature [51]. Cerro *et al.* derived the following distribution parameters for  $n_0$  and  $\Lambda$  as a function of the precipitation rate:  $n_0 = 2.32 \cdot 10^3 R_p^{0.22}$  and  $\Lambda = 3.32 R_p^{-0.18}$ . By setting  $R_p = 1 \text{ mm/h}$ ,  $n_0$  is  $2320 \text{ m}^{-3} \text{ mm}^{-1}$  and  $\Lambda$  is  $3.32 \text{ mm}^{-1}$ . The obtained parameters for rain and snow in the present study are slightly lower than the values provided by Cerro *et al.* [51]. However, the derived distribution parameters represent the entire measured size distributions for a given precipitation type during the transmission experiments. This also includes weather conditions with precipitation rates smaller than 1 mm/h. In the case of drizzle/rain, a detailed comparison of the distribution parameters cannot be made.

#### E. Comparison of Measured and Calculated Extinction Coefficients

An estimate of the optical thickness  $\tau$  based on the maximum measured extinction coefficient (on a one-minute basis) and the path length yields  $\tau = 2.44 \text{ km}^{-1} \cdot 0.13 \text{ km} = 0.31$ . The estimated optical thickness is slightly above the value of 0.1, which is often viewed as the onset of multiple scattering effects [52]. In the literature, an optical thickness of 1 is also considered to be



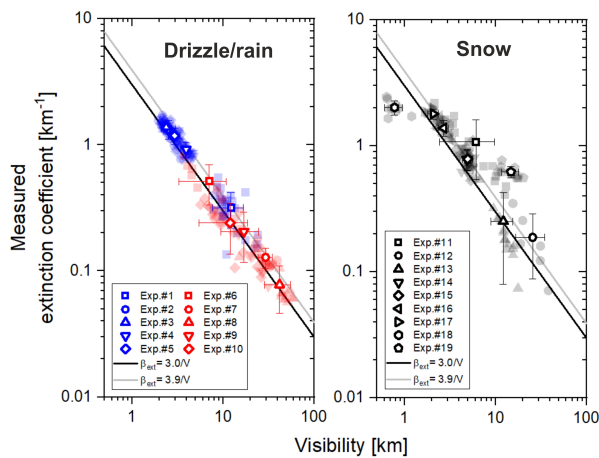


**Fig. 6.** Measured extinction coefficients as a function of visibility for drizzle/rain (blue) and rain (red) in the left panel and snow (black) in the right panel. The transparent and open symbols are integrated one-minute measurements and arithmetic mean values for each measurement series, respectively. The bold black line is the Koschmieder line in both panels. The error bars denote  $\pm 1$  standard deviation.

the starting point of multiple scattering [17,53]. Therefore, it cannot be completely ruled out that a certain amount of multiple scattering occurs at high extinction values. In the following, only a correction of the extinction coefficient due to forward-scattered radiation is included (see Section 2). The extinction coefficients are calculated based on the measured number size distributions of precipitation particles and geometric optics according to Eq. (5). The correction for forward-scattering of precipitation particles is performed using Eq. (6). The calculation of the extinction coefficients of aerosol particles is described in more detail in Appendix B. The averaged size distributions of aerosol particles for each measurement series are also provided in Appendix B (see Fig. 10).

Figures 7 and 8 show the comparison between the measured and calculated extinction coefficients for the different precipitation types. In each figure, the calculated extinction coefficients without and with forward-scattering correction are plotted on the abscissa in the left and right panels, respectively. In Fig. 7, the measured and uncorrected calculated extinction coefficients agree quite well, as indicated by an rms error (RMSE) value of 0.16. The inclusion of the forward-scattering correction slightly reduces the agreement and thus increases the RMSE value ( $\text{RMSE} = 0.19$ ). On the other hand, the agreement between the measured and uncorrected calculated extinction coefficients in snow is low ( $\text{RMSE} = 0.97$ ), compared to the calculated extinction coefficients with the forward-scattering correction included ( $\text{RMSE} = 0.29$ ). The forward-scattering correction is expected to be more pronounced for snow than for drizzle and rain due to the different shapes of the particle size distributions (see Section 4.D). Note that the calculated extinction coefficient is more corrected for snow than for drizzle and rain, as shown in Figs. 7 and 8.

The deviations at the high end (i.e., high extinction coefficients) can be attributed to the contribution of forward-scattered radiation into the receiver's FOV. By including the forward-scattering correction, a significantly better agreement

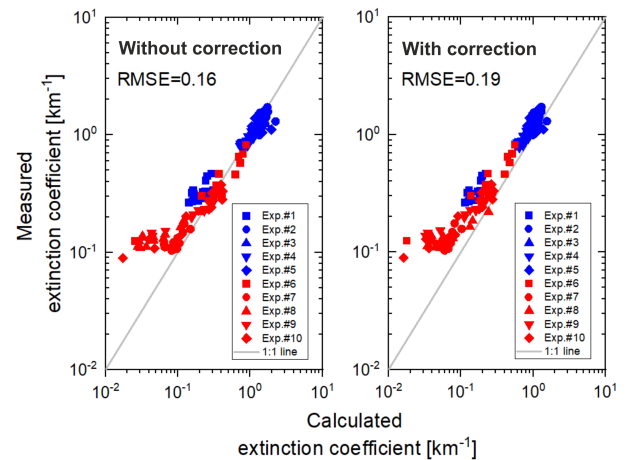


**Fig. 7.** Measured extinction coefficient for drizzle/rain and rain as a function of the calculated extinction coefficient for drizzle/rain and rain without forward-scattering correction (left panel) and with forward-scattering correction (right panel). The blue and red colors denote the transmission measurements during drizzle/rain and rain, respectively. The straight gray line indicates the 1:1 relation.

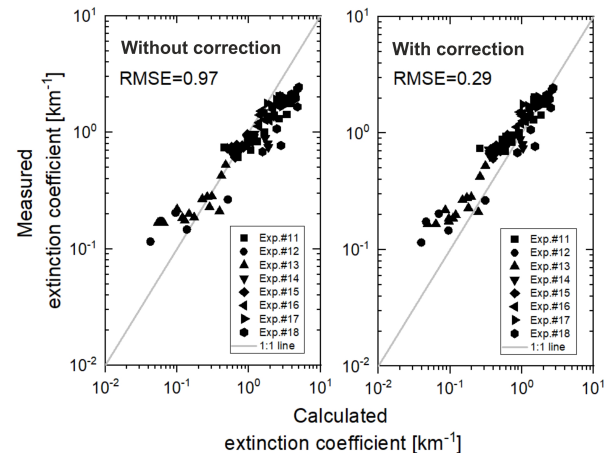


**Fig. 8.** Measured extinction coefficient for snow as a function of the calculated extinction coefficient for snow without forward-scattering correction (left panel) and with forward-scattering correction (right panel). The straight gray line indicates the 1:1 relation.

can be obtained for snow, as shown in the right panel of Fig. 8. The deviations at the lower end are likely due to the spatially inhomogeneous distribution of precipitation along the propagation path [4]. Due to the variability of precipitation during the experiments, the number concentration of particles at the site of the Thies laser precipitation monitor may be different from that over the entire propagation path. Another reason for the discrepancy could be that the LPM instrument underestimates the number of small particles in the size range between 0.5 and 3.5  $\mu\text{m}$  more in rain compared to snow [21]. Since this size range accounts for a large part of the total rain volume, this could also affect the calculation of the extinction coefficients. In view of obtained measurement results and calculations, note that:

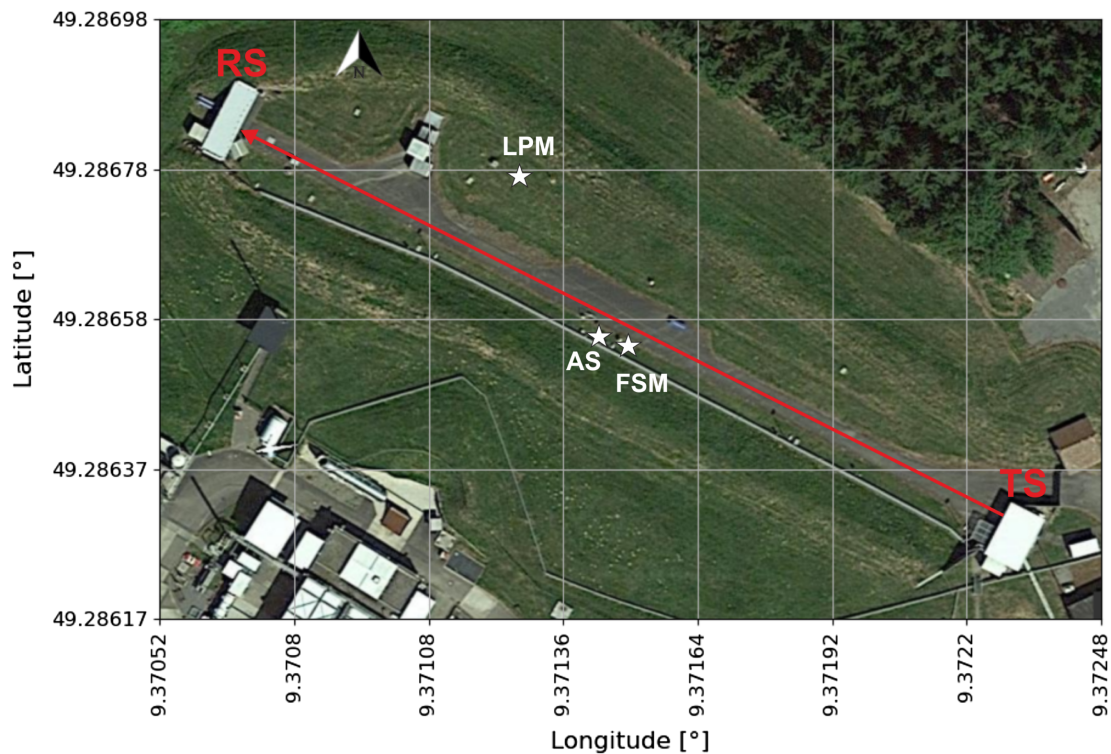


**Fig. 9.** Geographic map of the DLR laser test range at Lampoldshausen. The white stars indicate the locations of the atmospheric sensing instruments used in this study. TS, transmitting station; RS, receiving station; LPM, laser precipitation monitor; FSM, forward scatterometer; and AS, aerosol spectrometer. Source: Google Earth (2021), GeoBasis-DE/BKG (2009).

1. The molecular extinction coefficient is in the range of  $1.31 \cdot 10^{-3} - 1.98 \cdot 10^{-3} \text{ km}^{-1}$  depending on the water vapor content and temperature. The aerosol extinction coefficient is in the range of  $3.13 \cdot 10^{-4} - 1.71 \cdot 10^{-2} \text{ km}^{-1}$  based on the measured particle size distributions and Mie calculations. Therefore, the contribution of molecules and aerosols to the total extinction coefficient is relatively small.
2. The presence of fog during the transmission experiments in snow cannot be ruled out. However, the forward scatterometer (FSM) indicates that no fog was present during the measurements (see Section 3.B).
3. The contribution of multiple scattering is estimated to be small and occurred at most for the highest measured extinction coefficients (see Section 4.E).
4. An open detector system is used in the transmission experiments, which results in a significant amount of forward-scattered radiation being received by the detector, so an appropriate correction based on Fraunhofer diffraction theory is applied [10,24].
5. Laser transmission and visibility measurements indicate that the wavelength has only a minor influence (see Section 4.C). Due to the detection geometry, a non-negligible wavelength dependence of the extinction coefficient can result from the forward-scattering of precipitation particles [10,16,17].

## 5. SUMMARY

Atmospheric laser transmission experiments at  $1.03 \text{ }\mu\text{m}$  are performed on the DLR laser test range at Lampoldshausen under various weather conditions including drizzle/rain, rain, and snow. Experimental extinction coefficients are derived and related to observable weather parameters such as precipitation rate, visibility, and the number size distribution of precipitation particles. The relationship between the measured extinction coefficients for rain and liquid precipitation rate is found to be consistent with results in the literature. For a given precipitation rate of  $\sim 1 \text{ mm/h}$ , the extinction coefficients for drizzle/rain are higher by a factor of four compared to rain. For snow, extinction coefficients are a factor of seven higher than for rain. In the case of mixed precipitation (i.e., rain and snow), extinction coefficients comparable to those for rain are observed. This implies that the liquid precipitation rate can be used to estimate the extinction coefficient for drizzle and rain if the precipitation types can be distinguished using the SYNOP weather code, whereas the solid precipitation rate is subject to larger uncertainties due to the variability in snow particle mass densities and particle size distributions of individual snow events. The observed relationship between the extinction coefficient and visibility proved that the Koschmieder equation can be used to estimate the extinction coefficient at  $1.03 \text{ }\mu\text{m}$ , although the observed visibility data for snow exhibited a larger scatter. The relationship between the measured extinction coefficients and the calculated extinction coefficients based on number size distributions and geometric optics showed a good agreement

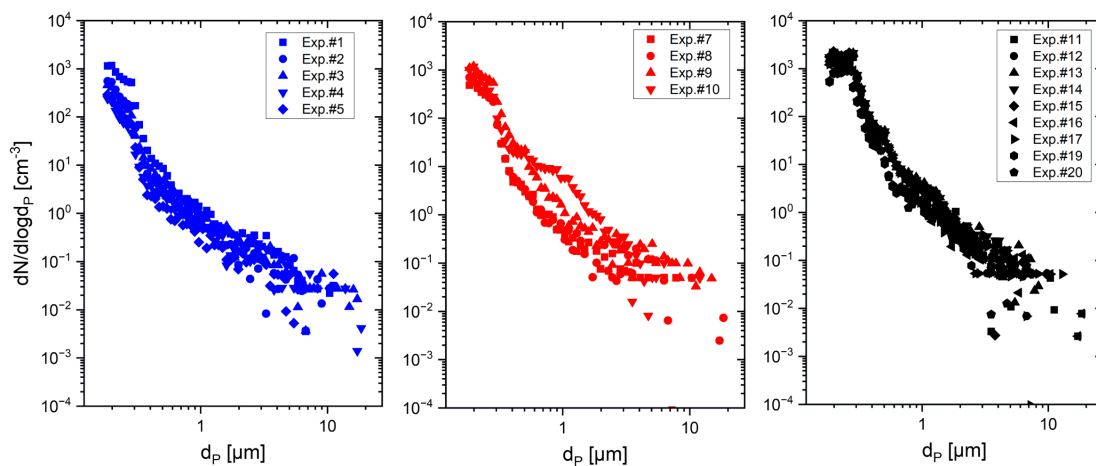


**Fig. 10.** Number size distributions of aerosol particles measured under different precipitation conditions. Left panel: drizzle/rain; middle panel: rain; and right panel: snow.

for rain, with the inclusion of the forward-scattering correction slightly reducing the agreement. On the other hand, the agreement between the measured and calculated uncorrected extinction coefficients for snow is poor and the inclusion of the forward-scattering correction led to a clear improvement of the RMSE value.

A more accurate estimate of the extinction coefficient in snow would be possible with a detailed analysis of the snow type; for example, by collecting and replicating snow particles or by using in-situ imaging techniques (such as a 2D video distrometer [46]) to determine the shape and type of snow crystals. Since the calculated extinction value relies on measured (truncated) size distributions, an approach that combines the size distributions from different instruments across the entire spectrum of atmospheric particles, including aerosol particles, fog droplets, and precipitation, could provide insight into their individual contributions and allow the application of appropriate correction methods. Likewise, recording particle size distributions at more than one location along the propagation path would provide additional information about spatial inhomogeneity on small scales. It can be concluded that the measured size distributions of atmospheric particles in combination with geometric optics and necessary corrections provide a better estimate for the extinction than integrated weather parameters such as the precipitation rate.

## APPENDIX A: METEOROLOGICAL INSTRUMENTATION

Figure 9 shows the laser test range of the DLR Institute of Technical Physics at the Lampoldshausen site. The positions of the meteorological instruments relevant for this study are marked on the geographic map. Weather data are recorded continuously (24/7) by the instruments.

## APPENDIX B: AEROSOL PARTICLE DATA

The extinction coefficients of aerosol particles are calculated according to Eq. (5). The extinction efficiencies are determined using the established Mie scattering code of Wiscombe [54]. An

effective complex refractive index of  $1.520 - 0.014i$  (reported for  $1.06 \mu\text{m}$ ) is used, which is representative of rural aerosol particles [55]. The wavelength for the Mie calculations is set to  $1.03 \mu\text{m}$ . The input data for the calculations are the measured number size distributions provided by the aerosol spectrometer. For the sake of comparability, average values are derived from the measured one-minute aerosol particle size distributions for each measurement series, and the size distributions are normalized with respect to the instrument-specific bin widths, as shown in Fig. 10.

**Acknowledgment.** The authors would like to thank Björn Prietzel, Thomas Schlagenhauser, and Ralf Zimmermann for their technical support of the experiments and Kirsten Klaffki for the preparation of the meteorological data.

**Disclosures.** The authors declare no conflicts of interest.

**Data availability.** Data underlying the results presented in this paper are not publicly available at this time but may be obtained from the authors upon reasonable request.

## REFERENCES

1. D. L. Hutt, J.-M. Theriault, V. Laroche, P. Mathieu, and D. Bonnier, "Estimating atmospheric extinction for eyesafe laser rangefinders," *Opt. Eng.* **33**, 3762–3773 (1994).
2. G. C. Holst, *Electro-Optical Imaging System Performance*, 6th ed. (JCD Publishing, 2017).
3. S. Mori and F. S. Marzano, "Microphysical characterization of free space optical link due to hydrometeor and fog effects," *Appl. Opt.* **54**, 6787–6803 (2015).
4. M. Rahm, P. Jonsson, and M. Henriksson, "Laser attenuation in falling snow correlated with measurements of snow particle size distribution," *Opt. Eng.* **60**, 094102 (2021).
5. B. Zohuri, *Directed Energy Weapons—Physics of High Energy Lasers (HEL)*, 1st ed. (Springer International Publishing Switzerland, 2016).
6. S. Affan Ahmed, M. Mohsin, and S. M. Zubair Ali, "Survey and technological analysis of laser and its defense applications," *Def. Technol.* **17**, 583–592 (2021).
7. T. S. Chu and D. C. Hogg, "Effects of precipitation on propagation at 0.63, 3.5, and 10.6 microns," *Bell Syst. Tech. J.* **47**, 723–759 (1968).
8. V. Chimelis, "Extinction of CO<sub>2</sub> laser radiation by fog and rain," *Appl. Opt.* **21**, 3367–3372 (1982).
9. D. B. Rensch and R. K. Long, "Comparative studies of extinction and backscattering by aerosols, fog, and rain at 10.6  $\mu\text{m}$  and 0.63  $\mu\text{m}$ ," *Appl. Opt.* **9**, 1563–1573 (1970).



10. H. Vasseur and C. J. Gibbins, "Prediction of apparent extinction for optical transmission through rain," *Appl. Opt.* **35**, 7144–7150 (1996).
11. L. Winchester and G. Gimmestad, "Propagation of visible and infrared radiation in fog, rain, and snow," Tech. Rep. (Keweenaw Research Center, Michigan Technological University, 1982).
12. C. W. Ulbrich and D. Atlas, "Extinction of visible and infrared radiation in rain: Comparison of theory and experiment," *J. Atmos. Ocean. Technol.* **2**, 331–339 (1985).
13. C. D. Stow, S. G. Bradley, K. Paulson, and L. Couper, "The simultaneous measurement of rainfall intensity, drop-size distribution, and the scattering of visible light," *J. Appl. Meteorol. Climatol.* **30**, 1422–1435 (1991).
14. M. A. Seagraves, "Precipitation rate and extinction in falling snow," *J. Atmos. Sci.* **41**, 1827–1835 (1984).
15. M. A. Seagraves, "Visible and infrared extinction in falling snow," *Appl. Opt.* **25**, 1166–1169 (1986).
16. G. Koh, "Physical and optical properties of falling snow," Tech. Rep. (Cold Regions Research and Engineering Laboratory (CRREL), 1989).
17. D. L. Hutt, L. R. Bissonnette, D. S. Germain, and J. Oman, "Extinction of visible and infrared beams by falling snow," *Appl. Opt.* **31**, 5121–5132 (1992).
18. D. Atlas, "Optical extinction by rainfall," *J. Atmos. Sci.* **10**, 486–488 (1953).
19. S. T. Shipley, E. W. Eloranta, and J. A. Weinman, "Measurement of rainfall rates by lidar," *J. Appl. Meteorol. Climatol.* **13**, 800–807 (1974).
20. H. W. O'Brien, "Visibility and light attenuation in falling snow," *J. Appl. Meteorol. Climatol.* **9**, 671–683 (1970).
21. M. Fehlmann, M. Rohrer, A. von Lerber, and M. Stoffel, "Automated precipitation monitoring with the Thies disdrometer: biases and ways for improvement," *Atmos. Meas. Tech.* **13**, 4683–4698 (2020).
22. J. B. Mason, "Light attenuation in falling snow," Tech. Rep. ASL-TR-0018 (US Army Atmospheric Sciences Laboratory, 1978).
23. H. Koschmieder, *Theorie der horizontalen Sichtweite*, Beiträge zur Physik der freien Atmosphäre (1924).
24. A. Deepak and M. A. Box, "Forwardscattering corrections for optical extinction measurements in aerosol media. 1: Monodispersions," *Appl. Opt.* **17**, 2900–2908 (1978).
25. L. Wind and W. W. Szymanski, "Quantification of scattering corrections to the Beer-Lambert law for transmittance measurements in turbid media," *Meas. Sci. Technol.* **13**, 270 (2002).
26. J. Guo and X.-J. Zhao, "Attenuation characterization of 532 nm and 1064 nm laser propagating in rain," *Optik* **127**, 9088–9094 (2016).
27. Harvard-Smithsonian Center for Astrophysics (CFA), V.E. Zuev Institute of Atmospheric Optics (IAO), and National Research Tomsk State University (TSU), "Hitran on the web information system," <https://hitran.iao.ru/>. Retrieved August 10, 2023.
28. J. H. Seinfeld and S. N. Pandis, *Atmospheric Chemistry and Physics*, 3rd ed. (Wiley, 2006).
29. C. F. Bohren and D. R. Huffman, *Absorption and Scattering of Light by Small Particles* (Wiley, 1983).
30. P. Räisänen, A. Kokhanovsky, G. Guyot, O. Jourdan, and T. Nousiainen, "Parameterization of single-scattering properties of snow," *Cryosphere* **9**, 1277–1301 (2015).
31. K. V. Beard, V. Bringi, and M. Thurai, "A new understanding of rain-drop shape," *Atmos. Res.* **97**, 396–415 (2010).
32. A. A. Kokhanovsky and E. P. Zege, "Scattering optics of snow," *Appl. Opt.* **43**, 1589–1602 (2004).
33. C. F. Bohren and G. Koh, "Forward-scattering corrected extinction by nonspherical particles," *Appl. Opt.* **24**, 1023–1029 (1985).
34. A. Guyot, J. Pudashine, A. Protat, R. Uijlenhoet, V. R. N. Pauwels, A. Seed, and J. P. Walker, "Effect of disdrometer type on rain drop size distribution characterisation: a new dataset for south-eastern Australia," *Hydrol. Earth Syst. Sci.* **23**, 4737–4761 (2019).
35. L. Liao, R. Meneghini, T. Iguchi, and A. Detwiler, "Use of dual-wavelength radar for snow parameter estimates," *J. Atmos. Ocean. Technol.* **22**, 1494–1506 (2005).
36. R. P. de Moraes Frasson, L. K. da Cunha, and W. F. Krajewski, "Assessment of the Thies optical disdrometer performance," *Atmos. Res.* **101**, 237–255 (2011).
37. Z. Lee and S. Shang, "Visibility: how applicable is the century-old Koschmieder model?" *J. Atmos. Sci.* **73**, 4573–4581 (2016).
38. A. Peckhaus, T. Hall, C. Pargmann, and F. Duschek, "Modelling studies of transmission and scattering of high energy laser radiation under remote continental conditions," *Proc. SPIE* **10787**, 107870G (2018).
39. C. Pargmann, T. Hall, F. Duschek, and J. Handke, "Atmospheric propagation of high power laser radiation at different weather conditions," *Proc. SPIE* **9833**, 983302 (2016).
40. PRIMES GmbH, "Original instructions—CompactPowerMonitor (CPM)," Revision 05 EN-08/2021, <https://www.primes.de/en/products/laser-power/continuous-radiation/compactpowermonitor-cpm.html>.
41. Adolf Thies GmbH & Co. KG, "Instruction for use—laser precipitation monitor 5.4110.xx.x00," (2022). V2.7x STD, [https://www.thiesclima.com/db/dnl/5.4110.xx.x00\\_Laser\\_Precipitation\\_Monitor\\_eng.pdf](https://www.thiesclima.com/db/dnl/5.4110.xx.x00_Laser_Precipitation_Monitor_eng.pdf).
42. Biral, "Operation and maintenance manual—VPF present weather sensors," (2014). Revision: 08E, <https://www.biral.com/wp-content/uploads/2019/07/VPF-710-730-750-Manual-102186.08E.pdf>.
43. World Meteorological Organization (WMO), "Manual on Codes—International Codes Volume I.1 Annex II to the WMO Technical Regulations Part A—Alphanumeric Codes, No. 306," (2019), [https://library.wmo.int/index.php?lvl=notice\\_display&id=13617](https://library.wmo.int/index.php?lvl=notice_display&id=13617).
44. American Meteorological Society, "Rain," in the *Glossary of Meteorology* (2021), <http://glossary.ametsoc.org/wiki/rain>.
45. I. Gultepe and J. A. Milbrandt, "Probabilistic parameterizations of visibility using observations of rain precipitation rate, relative humidity, and visibility," *J. Appl. Meteorol. Climatol.* **49**, 36–46 (2010).
46. M. Thurai, P. Gatlin, V. N. Bringi, W. Petersen, P. Kennedy, B. Notaroš, and L. Carey, "Toward completing the raindrop size spectrum: Case studies involving 2D-video disdrometer, droplet spectrometer, and polarimetric radar measurements," *J. Appl. Meteorol. Climatol.* **56**, 877–896 (2017).
47. C. Ulbrich and D. Atlas, "A method for measuring precipitation parameters using radar reflectivity and optical extinction," *Ann. Télécommun.* **32**, 415–421 (1977).
48. D. C. Blanchard, "Raindrop size-distribution in Hawaiian rains," *J. Atmos. Sci.* **10**, 457–473 (1953).
49. R. Nebuloni and C. Capsoni, "Laser attenuation by falling snow," in *6th International Symposium on Communication Systems, Networks and Digital Signal Processing* (2008), pp. 265–269.
50. J. S. Marshall and W. M. K. Palmer, "The distribution of raindrops with size," *J. Atmos. Sci.* **5**, 165–166 (1948).
51. C. Cerro, B. Codina, J. Bech, and J. Lorente, "Modeling raindrop size distribution and z(r) relations in the western Mediterranean area," *J. Appl. Meteorol.* **36**, 1470–1479 (1997).
52. H. C. van de Hulst, *Light Scattering by Small Particles* (Wiley, 1957).
53. L. Ma, J. Zhai, and C. Wang, "Investigation of the single scattering approximation through direct electromagnetic scattering simulation," *OSA Contin.* **4**, 2496–2509 (2021).
54. W. J. Wiscombe, "Improved Mie scattering algorithms," *Appl. Opt.* **19**, 1505–1509 (1980).
55. G. S. Kent, G. K. Yue, U. O. Farrukh, and A. Deepak, "Modeling atmospheric aerosol backscatter at CO<sub>2</sub> laser wavelengths. 1: Aerosol properties, modeling techniques, and associated problems," *Appl. Opt.* **22**, 1655–1665 (1983).